ARTICLE

Designing Chemically Selective Liquid Crystalline Materials that Respond to Oxidizing Gases

Received 00th January 20xx,
Accepted 00th January 20xx

DOI: 10.1039/x0xx00000x

Nanqi Bao,[†,a] Jake I. Gold, [†,b] Tibor Szilvási,[b] Huaizhe Yu,[a] Robert J. Twieg,[c] Manos Mavrikakis,[*,b] and Nicholas L. Abbott[*,a]

Computational methods can provide first-principles insights into the thermochemistry and kinetics of reactions at interfaces, but this capability has not been widely leveraged to design soft materials that respond selectively to chemical species. Here we address this opportunity by demonstrating the design of micrometer-thick liquid crystalline films supported on metal-perchlorate surfaces that exhibit selective orientational responses to targeted oxidizing gases. Initial electronic structure calculations predicted Mn^{2+}, Co^{2+} and Ni^{2+} to be promising candidate surface binding sites that (1) coordinate with nitrile-containing mesogens to orient liquid crystal (LC) phases and (2) undergo redox-triggered reactions upon exposure to humid O_3 leading to a change in the strength of binding of the nitrile group to the surface. These initial predictions were validated by experimental observations of orientational transitions of nitrile-containing LCs upon exposure to air containing parts-per-billion concentrations of O_3. Additional first-principles calculations of reaction free energies of metal salts and oxidizing gases predicted that the same set of metal cations, if patterned on surfaces at distinct spatial locations, would provide LC responses that allow Cl_2 and O_3 to be distinguished while not responding to environmental oxidants such as O_2 and NO_2. Experimental results are provided to support this prediction, and X-ray diffraction measurements confirmed that the experimentally observed LC responses can be understood in terms of the relative thermodynamic driving force for formation of MnO_2, CoOOH, or NiOOH from the corresponding metal cation binding sites in the presence of humid O_3 and Cl_2.

1. Introduction

The liquid crystalline state of matter possesses fluid-like mobility and long-range orientational order.[1] This combination of properties underlies the responsiveness of liquid crystals (LCs) to external electric fields, which is widely used in a electrooptical devices.[2,3] More recently, LCs have been designed as materials that respond to chemical stimuli (chemoresponsive materials).[4–8] In one strategy, the orientations of molecules (mesogens) within LCs are changed by non-covalent interactions between the LC and chemical functional groups presented at surfaces.[5,9–12] Such chemoresponsive LC materials form the basis of a promising approach for sensing targeted chemical species such as volatile organic compounds (e.g., toluene)[13,14], biomolecules (proteins or oligonucleotides)[4,15–19], or toxic gaseous species (e.g., organophosphonates[5,20–24]). In this paper, we focus on the design of chemoresponsive LC materials for oxidizing gases.

Past studies have shown that mesogens with specific functional groups (e.g. nitrile or pyrimidine) can bind to metal cations, deposited on surfaces as perchlorate or nitrate salts, to cause homeotropic (perpendicular to surface) anchoring of LC materials.[22,24] The bound mesogens can be displaced by a stronger binding molecule (analyte) such as an organophosphonate to trigger a change in the LC orientation (to planar (parallel to surface) anchoring).[5,20–24] These studies also showed that first principles calculations can be used to predict if the initial homeotropic anchoring of the mesogen is favored via the evaluation of the binding free energy [22,25,26]. In addition, a response of the LC to a targeted compound was predicted for the case where displacement of the mesogen by the analyte was strongly favored by a decrease in free energy. In this paper, we use electronic structure calculations to guide the design of LC materials that respond selectively to oxidizing gases.

The approach reported here builds from our previous design of a LC system that responded to chlorine (Cl_2) gas.[27] In contrast to the displacement reactions used for targeted compounds that bind strongly to metal cations (e.g., DMMP), Cl_2 binds weakly to metal cations and thus cannot be detected via displacement of a mesogen coordinated to a metal cation.[27] We established, however, that oxidation of the Mn^{2+} cation by Cl_2 in the presence of water vapor generated MnO_2, which binds the LC weakly and triggers an orientational transition that can be optically transduced. In this paper, we describe an integrated computational/experimental study that aimed to design LCs that respond selectively to oxidizing gases other than Cl_2. We

[a.] *Robert Frederick Smith School of Chemical and Biomolecular Engineering, Cornell University, 1 Ho Plaza, Ithaca, New York 14853, USA.*
[b.] *Department of Chemical and Biological Engineering, University of Wisconsin-Madison, 1415 Engineering Drive, Madison, Wisconsin 53706, USA.*
[c.] *Department of Chemistry and Biochemistry, Kent State University, 1175 Risman Drive, Kent, Ohio 44242, USA.*
† Authors contributed equally to this work.
Electronic Supplementary Information (ESI) available: [details of any supplementary information available should be included here]. See DOI: 10.1039/x0xx00000x

focus on ozone gas (O_3), an environmentally and industrially important gas[28–30], and designs of LC materials that permit selective detection of O_3 versus Cl_2 in the presence of O_2 and NO_2.

A number of methodologies have been reported for detection of O_3, including gas chromatography[31], electrochemical methods[32,33] or approaches based on changes in the conductivity of semiconductors.[34–37] These methods, however, are not suitable as the basis of wearable sensors for monitoring of personal exposure to O_3 because they possess one or more of the following limitations: they require active sampling methods (pumps; >1 L/min)[31], involve complex and large instruments[31–37] (e.g., spectrometers), require gas pretreatment (separation)[31–33], require electrical power[31–37] or operate at elevated temperatures[36,37]. We seek to advance approaches that have the potential to overcome these limitations by development of chemoresponsive LCs. The effort is motivated by prior demonstrations that chemoresponsive LCs, if successfully developed for a targeted analyte, can be integrated into passive (no electrical power), lightweight and wearable devices for monitoring of personal exposure.[38] Beyond monitoring of personal exposure to O_3, the attributes of chemoresponsive LCs (lightweight, passive) makes them an attractive option of atmospheric monitoring using aerial drones or balloons.[39] Here we emphasize, however, that development of chemoresponsive LCs for a target such as O_3 requires not only that the LC responds to O_3 but also that it not respond to other oxidizing gases (e.g. Cl_2, NO_2, O_2). For example, a chemoresponsive LC intended for workplace monitoring of O_3 in a water treatment facility will need to be able to differentiate between O_3 and Cl_2 because both are widely used together for wastewater treatment and drinking water disinfection.[28]

Our design of a chemoresponsive LC that is selective for O_3 is based on the strong oxidizing potential of O_3.[40 41–43]. In particular, O_3 has been reported to oxidize Co^{2+} [44–47] and Ni^{2+} [45] to the 3+ oxidation state in aqueous solution, with the products being CoOOH and NiOOH, respectively. Moreover, Bardé et al. demonstrated the synthesis of CoOOH[48] and NiOOH[49] by oxidation of solid $Co(OH)_2$ and $Ni(OH)_2$ by O_3 in the presence of water vapor, with the final products (CoOOH and NiOOH) characterized by XRD. Motivated by these prior experimental studies, we pursued an integrated computational-experimental approach to selective detection of O_3 and Cl_2 by anchoring LCs on surfaces presenting Mn^{2+}, Co^{2+}, and Ni^{2+} perchlorate salts.

For the case studied here with O_3 oxidation of Ni^{2+} and Co^{2+}, the relevant redox half reactions have not been reported in the literature. This observation required that we develop a new approach in which we calculated, using first principles methods, the reaction free energies that lead to formation of bulk oxides (MnO_2) and bulk oxyhydroxides (CoOOH, NiOOH) from bulk perchlorate salts ($Mn(ClO_4)_2$, $Co(ClO_4)_2$, $Ni(ClO_4)_2$). These reaction free energies led us to predict whether or not specific LC designs would respond to O_3, Cl_2, O_2, or NO_2, predictions that we validated using experiments. We also explore experimental observations of dynamic responses of LC materials using a simple kinetic model that describes transport and reaction of the analytes with the metal salts[50]. We find that the dynamic response of the LC is limited by diffusion of O_3 and Cl_2 across the LC film. Overall, the study reported in this paper advances a first-principles-based methodology for the design of chemically selective LC materials.

2. Methods

2.1 Theoretical

All bulk, surface, and cluster calculations were performed using Density Functional Theory as implemented in Vienna Ab Initio Simulation Package (VASP) code.[51,52] Projector augmented wave potentials were used to describe the electron-ion interactions.[53,54] The exchange-correlation functional was described by the generalized gradient approximation (GGA-PBE).[55] Dispersion corrections were used in all calculations employing Grimme's D3 empirical dispersion correction scheme with zero damping.[56] All calculations were performed spin-polarized. Onsite Coulomb correlation of the occupied transition metal d states is corrected with the DFT+U[57,58] approach using Hubbard type parameters of 5.5, 3.9, and 3.5 for Ni[59], Mn[60], and Co[61], respectively. The electron wave function was expanded using plane waves with an energy cutoff of 520 eV. The Brillouin zone (BZ) was sampled with Γ-centered Monkhorst–Pack k-point mesh[62] with a k-point density greater than 80 k-points per 1/Å for bulk calculations. For example, an 18 x 18 x 28 k-point mesh was sampled for bulk rutile β-MnO_2, which has a unit cell size of 4.48 Å x 4.46 Å x 2.98 Å. Only the Γ-point was sampled for binding and binding free energy calculations for surface and cluster calculations. Gaussian smearing of 0.1 eV was used in all calculations. Structures were relaxed until the Hellmann–Feynman forces acting on each atom were less than 0.02 eV $Å^{-1}$.

The binding energy (E_B) of a species adsorbing on a surface was calculated as:

$$E_B = E_{tot} - E_{gas} - E_{clean} \quad (1)$$

where E_{tot} is the total energy of the slab with the adsorbate on the surface, E_{gas} is the total energy of the gas-phase adsorbate, and E_{clean} is the total energy of the clean slab. By this definition, more negative values of E_B indicate stronger binding. Binding free energy (G_{BE}) is defined analogously. The binding energies and binding free energies for adsorption of 4'-*n*-pentyl-4-biphenylcarbonitrile (5CB) was calculated using the surrogate molecule benzonitrile (PhCN), which has been used previously.[24,63] The structures of 5CB and PhCN are shown in Figure 1. Additional details regarding the calculations can be found in the Electronic Supporting Information (ESI).

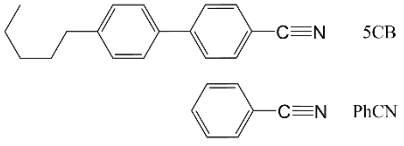

Figure 1. Molecular structure of 5CB and its surrogate benzonitrile (PhCN).

2.2 Experimental

Materials. Detailed information about sources of materials used in this study can be found in ESI.

Formation of thin films of LC supported on metal-salt-decorated surfaces. Glass slides were rinsed with copious amounts of ethanol and then dried under a stream of nitrogen. Metal ions were deposited onto the glass surfaces by spin coating ethanolic solutions of metal salts at the specified molar concentration (0.8-1.5 mM) at 3000 rpm for 30s (WS-400A-6NPP/Lite, Laurell Technologies, North Wales, PA). After coating the surface with the metal salt, an 18 µm-thick copper TEM grid (Electron Microscopy Sciences, Hatfield, PA) was placed on the metal-salt surface. The TEM grid was composed of squares with lateral dimensions of 285 µm and an overall diameter of 3 mm. The grids were filled with 0.1 µL LC using a microcapillary. The excess LC was removed from the grids by wicking the LC into an empty capillary tube.

O_3 and Cl_2 exposure. O_3 was generated and the concentration quantified, as described in ESI. Cl_2 was obtained from a certified cylinder containing 10 ppm. The relative humidities (RHs) of the flow streams were controlled using a dew point generator. (LI-610, LI-COR Biosciences, Lincoln, NE).

Measurement of the surface density of cation binding sites. To determine the density of metal cation binding sites, metal salts deposited on glass surfaces were dissolved into a 2% nitric acid solution. The concentration of the metal cations in solution was measured by using inductively coupled plasma optical emission spectrometry (ICP-OES, Perkin Elmer 4300). The surface density of the metal salt was calculated from both the ICP-OES data and knowledge of the area of the surface from which the metal salts were extracted. We note that this procedure yields only an apparent density of cation binding sites available to the mesogens, as some cations may be buried within the salt layer on the surface and thus not accessible to mesogens.

X-ray powder diffraction (XRPD). The metal salts were crushed to decrease the grain size below 100 µm. Next, the metal salt powder was transferred to a small quartz cuvette with a volume of 0.1 mL. XRPD patterns of the samples before and after O3 exposure were measured at room temperature using a Brucker D8 Discover Powder diffractometer (Brucker, Billerica, MA). The measurements were performed using Cu-Kα radiation with a wavelength of approximately λ=1.5406 Å and photon energy of E=8.04 keV. The scans covered the range of 10-80° with a step size of 0.019° in 2θ.

3. Results and discussion

3.1 LC anchoring on surfaces presenting select metal cation binding sites

3.1.1 Computational predictions

For nematic 5CB supported on a metal salt-decorated surface to exhibit an orientational transitions after exposure to an oxidizing gas, two criteria must be satisfied: (1) oxidation of the cation is thermodynamically favored, and (2) 5CB binding to the lower oxidation state of the cation is sufficiently strong to cause homeotropic anchoring while weak enough on the oxidized surface to cause planar anchoring. To evaluate if a LC orientational response could be designed for the new systems studied here, we first consider criterion (1) for O_3 and Cl_2 exposure to Mn^{2+}, Co^{2+}, and Ni^{2+} and subsequently discuss criterion (2).It is known that O_3 is a stronger oxidation agent than Cl_2. This can be understood by comparing the

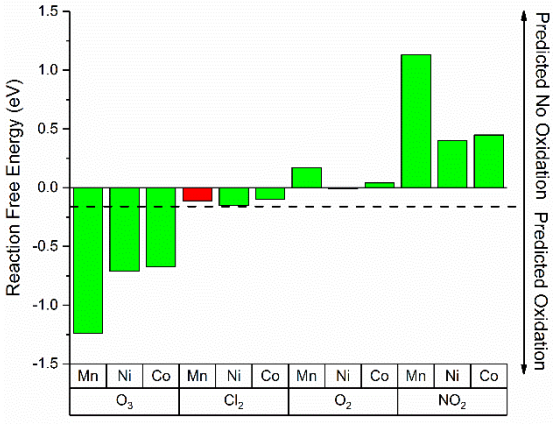

Figure 2. Calculated reaction free energies (ΔG) at relevant experimental conditions (1290 ppm O_3, 8 ppm Cl_2, 0.21 atm O_2, and 8 ppm NO_2 with 20% RH and 300K) using Equations 3-14. As detailed in the text, the green bars indicate agreement between theoretical predictions and experimental observations (of reactions leading to oxidized metal salt and an accompanying LC response), whereas a red bar shows disagreement. See ESI for more details on estimation of gas pressures of $HClO_4$, HCl, and NO.

redox potentials of O_3 to Cl_2 in Equation 1 and 2 in aqueous solution, where the O_3 oxidation potential is 0.72 V stronger than Cl_2.[64] Therefore, we predicted a faster response to O_3 on $Mn(ClO_4)_2$ as compared to Cl_2 gas, assuming these processes are reaction-limited.

$O_3 + 2H+ + 2e- \rightarrow O_2 + H_2O$ (E^0 = 2.076 V) (1)

$Cl_2(g) + 2e^- \rightarrow 2Cl^-$ (E^0 = + 1.358 V) (2)

Motivated by this information, we calculated the reaction free energies for O_3 and Cl_2 oxidation of Mn^{2+}, Co^{2+}, and Ni^{2+} in order to determine which cases are thermodynamically favored. In addition, we considered the free energies for reactions involving O_2 and NO_2 as these are ubiquitous potentially interfering compounds. The balanced equations for oxidation by O_3 are shown in Equations 3-5, Cl_2 in Equations 6-8, O_2 in Equations 9-11, and NO_2 in Equations 12-14 for Mn^{2+}, Co^{2+}, and Ni^{2+}, respectively. We write each equation with respect to the gas phase species and one mole of metal cation oxidized. To calculate reaction free energies, we assume a form for the oxidized product. O_3 exposure in the presence of water has been reported to produce MnO_2[40–43], $CoOOH$[44–48] and $NiOOH$[45,49], and Cl_2 exposure in the presence of water has been reported to produce MnO_2[65,66]. Therefore, we write Equations 3-14 with respect to these bulk species. All balanced reactions require water as a reactant; thus, we predict relative humidity (RH) to be necessary for a response in all cases.

$O_3(g) + H_2O(g) + Mn(ClO_4)_2 \rightarrow MnO_2 + O_2(g) + 2HClO_4(g)$ (3)

$0.5O_3(g) + 1.5H_2O(g) + Co(ClO_4)_2 \rightarrow CoOOH + 0.5O_2(g) + 2HClO_4(g)$ (4)

$0.5O_3(g) + 1.5H_2O(g) + Ni(ClO_4)_2 \rightarrow NiOOH + 0.5O_2(g) + 2HClO_4(g)$ (5)

$Cl_2(g) + 2H_2O(g) + Mn(ClO_4)_2 \rightarrow MnO_2 + 2HClO_4(g) + 2HCl(g)$ (6)

$0.5Cl_2(g) + 2H_2O(g) + Co(ClO_4)_2 \rightarrow CoOOH + 2HClO_4\ (g) + HCl(g)$ (7)

$0.5Cl_2(g) + 2H_2O(g) + Ni(ClO_4)_2 \rightarrow NiOOH + 2HClO_4(g) + HCl(g)$ (8)

$0.5O_2(g) + H_2O(g) + Mn(ClO_4)_2 \rightarrow 2HClO_4(g) + MnO_2$ (9)

$0.25O_2(g) + 1.5H_2O(g) + Co(ClO_4)_2 \rightarrow 2HClO_4(g) + CoOOH$ (10)

$0.25O_2(g) + 1.5H_2O(g) + Ni(ClO_4)_2 \rightarrow 2HClO_4(g) + NiOOH$ (11)

$NO_2(g) + H_2O(g) + Mn(ClO_4)_2 \rightarrow 2HClO_4(g) + MnO_2 + NO(g)$ (12)

$0.5NO_2(g)+1.5H_2O(g)+Co(ClO_4)_2 \rightarrow 2HClO_4(g)+CoOOH+0.5NO(g)$ (13)

$0.5NO_2(g)+1.5H_2O(g)+Ni(ClO_4)_2 \rightarrow 2HClO_4(g)+NiOOH+0.5NO(g)$ (14)

We tabulated the reaction free energies based on Equations 3-14 in Table S3, and plot a comparison of the values in Figure 2 at 300K for the following pressures: 1290 ppm O_3, 8 ppm Cl_2, 0.21 atm O_2, and 8 ppm NO_2 with 20% (additional details regarding estimations of pressures of $HClO_4$, HCl, and NO are found in the ESI). For O_3, we found that Mn^{2+} has the strongest thermodynamic driving force for oxidation (ΔG = -1.24 eV), followed by Ni^{2+} (ΔG = -0.71 eV), and Co^{2+} (ΔG = -0.67 eV); the latter two have similar reaction free energies. For all O_3 cases, the negative reaction free energies predict that the formation of oxidized species is strongly favored.

The reaction free energies are significantly less favored for Cl_2 gas as compared to O_3 gas, as indicated by Figure 2 (Table S3). For example, the most thermodynamically favored reaction free energy occurs for Ni^{2+} (ΔG = -0.15 eV) followed closely by Mn^{2+} (ΔG = -0.11 eV) and Co^{2+} (ΔG = -0.10 eV). Similar to the case for O_3, the reaction free energies for Cl_2 are all negative, indicating oxidation may be thermodynamically possible. However, the reaction free energies for Cl_2 are much smaller (more positive than -0.15 eV). Therefore, the thermodynamic driving force is much weaker for Cl_2 compared to O_3, and predictions regarding a LC response to Cl_2 are potentially within the error of our calculations.

The oxidation of these surfaces by O_2 and NO_2 are even less thermodynamically favored than for Cl_2. We find the reaction free energies are positive or very close to positive for O_2 on Mn^{2+} (+0.17 eV), Ni^{2+} (-0.01 eV), and Co^{2+} (+0.04 eV), indicating that oxidation may not be favored, and that a LC response is unlikely to occur with atmospheric levels of O_2. Similar results were found for NO_2, where all reaction free energies were calculated to be more positive than +0.40 eV. We note that a change in the reaction free energy of 0.06 eV corresponds to a 1 order of magnitude change in equilibrium constant at room temperature; thus, oxidation by NO_2 is not favored by about 7 orders of magnitude. Clearly the identity of the oxidizing species plays a central role in the underlying thermodynamics.

Inspection of Figure 2 reveals an additional trend: The reaction free energies for Co^{2+} and Ni^{2+} are similar for a given oxidizing gas because the gas stoichiometric coefficients in Equations 3-14 are the same for Co^{2+} and Ni^{2+} surfaces for each oxidant. In contrast, the gas stoichiometric coefficients for Mn^{2+} differ from Co^{2+} and Ni^{2+}, which leads to a change in reaction free energy that depends on the identity of the gas phase species.

To address criterion (2), that the oxidized product of the metal salt must bind sufficiently weakly to 5CB to cause a transition from homeotropic to planar orientation, we calculated binding free energies of nitrile-containing mesogens to low (LOS) and high oxidation states (HOS) of Mn, Co, and Ni salts shown in Table 1. For these calculations, we used PhCN as a surrogate molecule for 5CB (Figure 1). We found the binding free energy of PhCN to $Mn(ClO_4)_2$, $Co(ClO_4)_2$, and $Ni(ClO_4)_2$ to be -0.43 eV, -0.48 eV, and -0.52 eV, respectively (see also Figure 3a and Figure S2). In our past studies, we found that negative values of G_{BE} for mesogens adsorbed in a perpendicular orientation correlated with experimental observations of homeotropic anchoring.[22,24] The physical interpretation is that the negative value of G_{BE} selects the perpendicular alignment and that the orientation of the surface adsorbed mesogens is amplified into the bulk LC as homeotropic anchoring. We show here that all low oxidation states (LOS) have negative G_{BE} to PhCN, leading us to predict that homeotropic anchoring is preferred based on previous benchmark studies.[22,24] Next, we considered the case of the oxidized metal salts. As shown in Table 1, we found that PhCN prefers to bind in a parallel orientation to MnO_2 (+0.12 eV), CoOOH (-0.25 eV), and NiOOH (-0.22 eV): in contrast, the values of G_{BE} in the perpendicular alignment are more positive (weaker binding; Table S1). The mildly negative G_{BE} in parallel alignment on the oxidized surfaces of Ni and Co, mostly reflects the van der Waals interactions between the phenyl ring of PhCN and the oxidized metal surface, as these interactions are included in the DFT calculations by the Grimme's D3 corrections (Table S2 for more details). As an example, the structure of NiOOH is shown in Figure 3b, demonstrating that PhCN prefers parallel alignment on NiOOH (See Figure S2 for MnO_2 and CoOOH structures). Our physical interpretation of these results is that the parallel orientation of mesogens at the solid/LC interface on these oxidized salts will be amplified into planar anchoring in the bulk LC. Accordingly, we predicted that, if oxidation occurs, an anchoring transition of 5CB from homeotropic to planar would likely take place for all three metal cations studied.

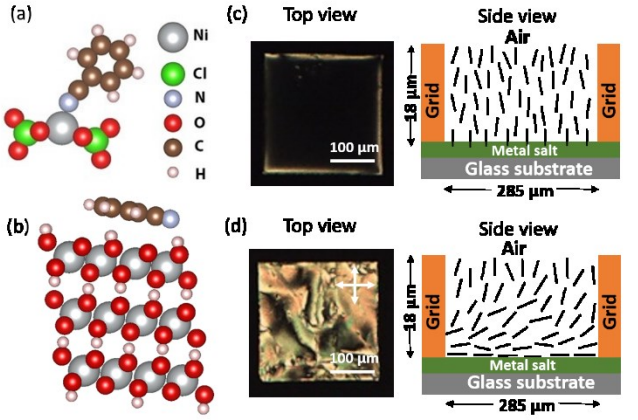

Figure 3. (a) Computational model used to predict the binding of 5CB to Ni^{2+} in the form of $Ni(ClO_4)_2$ (11 atom cluster) using PhCN as a surrogate molecule (24 atoms total with PhCN bound to cluster). (b) NiOOH slab (192 atoms) used to assess the orientation of 5CB on Ni^{3+} surfaces using PhCN as a surrogate molecule (205 atoms total in the model). (c) Optical image (crossed polarizers) of 5CB hosted in a copper grid (lateral size of grid square is 285 µm) on surface decorated with 15±2 pmol/mm^2 $Ni(ClO_4)_2$. Schematic illustration of the LC orientation is shown to the right of the image. (d) Optical image (crossed polarizers) of 5CB in a copper grid supported on a surface decorated with 15±2 pmol/mm^2 $Ni(ClO_4)_2$ and exposed to 1290±40 ppm O_3 (5 min at 20% RH) prior to contact with the 5CB.

Table 1. Calculated binding free energy (G_{BE} in eV) of PhCN, the surrogate of 5CB, to metal cations with low oxidation states (LOS) as perchlorate salts (2+ cations) and high oxidation states (HOS) in the form of oxyhydroxides (3+ cations) and oxide (4+ cation) surfaces.[a]

Cation (LOS/HOS)	LOS G_{BE} (eV)	HOS G_{BE} (eV)
Mn (2+/4+)	-0.43	+0.12
Co (2+/3+)	-0.48	-0.25
Ni (2+/3+)	-0.52	-0.22

[a]Entries for LOS column correspond to perpendicular alignment of PhCN; entries for HOS correspond to parallel alignment of PhCN (see ESI for additional details).

3.1.2 Experiments

To evaluate the above-described predictions in experiments, we decorated the surfaces of glass substrates with Mn^{2+}, Co^{2+}, and Ni^{2+} perchlorate salts at a similar metal cation surface density (~15 pmol/mm^2), which corresponds to >1 ML metal salt coverage, as established in our past study.[22] Figure 3c shows that 5CB adopted a homeotropic (perpendicular) orientation on $Ni(ClO_4)_2$ decorated surfaces when the LC was exposed to air (dark image between crossed polarizers). This observation is consistent with the computational prediction of strong binding between the nitrile group of 5CB, and the Ni^{2+} cation (-0.52 eV in Table 1), as discussed earlier. To examine 5CB anchoring on an O_3-exposed metal salt surface, we exposed a 15±2 pmol/mm^2 $Ni(ClO_4)_2$-decorated glass surface to 1290±40 ppm O_3 with 20% RH for 5 minutes, and then deposited 5CB on the surface. Figure 3d shows that the 5CB exhibited a bright optical appearance under crossed polarizers, indicating a parallel or tilted (non-homeotropic) orientation of 5CB on the solid surface after O_3 exposure. We determined the tilt angle of 5CB from the surface normal by measuring the optical retardance of 5CB in a LC cell composed of two identical O_3-exposed $Ni(ClO_4)_2$-decorated surfaces (Figure S4). The tilt angle was calculated to be 89±4° (details in ESI), consistent with parallel anchoring of PhCN on NiOOH, as predicted by DFT calculations (Figure 3b). Similar to the $Ni(ClO_4)_2$ system, we found that 5CB adopted a homeotropic orientation on the surfaces decorated with $Mn(ClO_4)_2$ and $Co(ClO_4)_2$ salts, and a planar orientation on the two surfaces following exposure to humid O_3 (Figure S2).

As an additional control experiment, we evaluated $Al(ClO_4)_3$-decorated glass substrates before and after exposure to humid O_3. We chose Al^{3+} because it is already in the highest oxidation state; therefore, it cannot be oxidized by O_3. In a previous study[22], we established that 5CB assumes a homeotropic orientation on $Al(ClO_4)_3$-decorated glass substrates. After exposure to humid O_3, we observed 5CB to maintain its perpendicular orientation (Figure S5). This result is consistent with the prediction that Al^{3+} cannot be oxidized by O_3.

Inspection of Equations 3-5 suggests that water is needed for metal-cation-oxidation reactions with O_3. Therefore, to further probe the proposed mechanism resulting in the LC orientational transition shown in Figure 3, we characterized the LC response to dry O_3 gas (<0.2% RH). We observed 5CB to maintain its perpendicular orientation on surfaces of $Mn(ClO_4)_2$, $Co(ClO_4)_2$,or $Ni(ClO_4)_2$ before and after treatment with dry O_3 (Figure S6). These results are consistent with the reported water-dependent oxidation of Mn^{2+}[43], Co^{2+}[48], and Ni^{2+}[49] cations. As an additional control experiment, we examined the response of 5CB on $Mn(ClO_4)_2$, $Co(ClO_4)_2$ or $Ni(ClO_4)_2$ to humidified N_2 gas. After 1 hour of exposure to 20% RH N_2, we observed 5CB to maintain its perpendicular orientation (Figure S6).

3.2 Characterization of metal-salt surfaces after O_3 exposure

To further establish that oxidation of the metal cations by humid O_3 is the cause of the LC orientation transition predicted by our computations, we characterized the metal salt-decorated surfaces before and after O_3 exposure by using X-ray diffraction (XRD). Our initial attempts to obtain XRD patterns from surfaces decorated with ~15 pmol/mm^2 metal perchlorate were not successful due to lack of signal. To address this issue, we used powder X-ray diffraction (PXRD) to characterize bulk

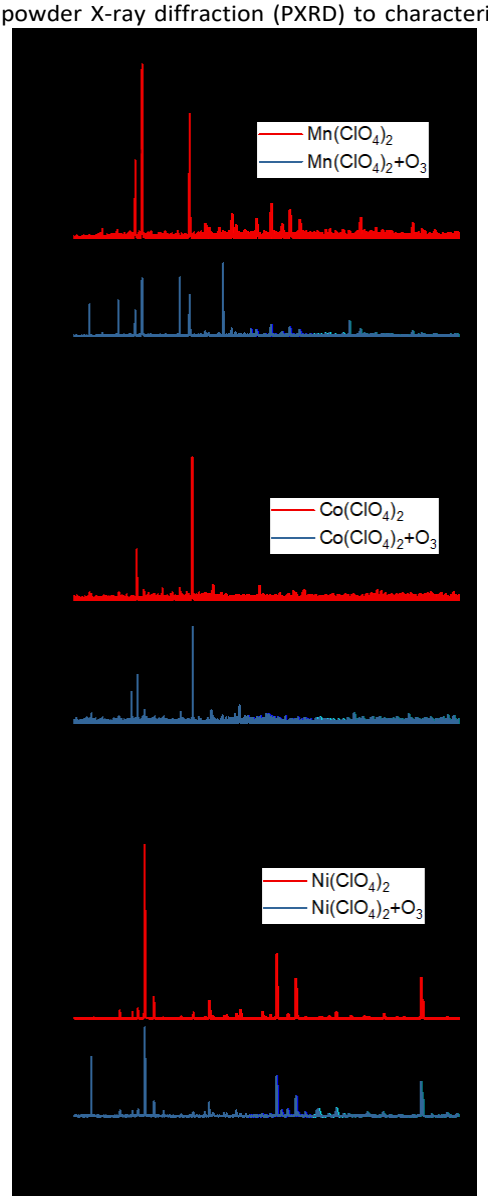

Figure 4. X-ray diffraction patterns of (a) $Mn(ClO_4)_2$, (b) $Co(ClO_4)_2$, and (c) $Ni(ClO_4)_2$ salts before (in red) and after 3-hour exposure to 1290±40 ppm O_3 with 20% RH (in blue). The characteristic peaks for metal perchlorates are labeled above the peaks with circles, and the characteristic peaks for MnO_2, CoOOH, or NiOOH are labeled above the peaks with asterisks.

$Mn(ClO_4)_2$, $Co(ClO_4)_2$, and $Ni(ClO_4)_2$ salts before and after humid O_3 exposure (Figure 4). The PXRD patterns for perchlorate salts are shown in red with their characteristic peaks labeled with circles. To validate our hypothesis regarding the formation of MnO_2, CoOOH, or NiOOH, the structures used in the computational predictions, we exposed $Mn(ClO_4)_2$, $Co(ClO_4)_2$ and $Ni(ClO_4)_2$ powders to humid O_3 (1290±40 ppm with 20% RH) for 3 hours and then characterized their PXRD patterns. PXRD patterns for O_3-exposed perchlorate salts are shown in blue with their characteristic peaks labeled with asterisks. Inspection of Figure 4 reveals that MnO_2, CoOOH or NiOOH formed with upon exposure of $Mn(ClO_4)_2$, $Co(ClO_4)_2$ or $Ni(ClO_4)_2$ salts powders, respectively to humid O_3. For example, for humid O_3-exposed $Mn(ClO_4)_2$ (Figure 4a), we identified α-MnO_2 from characteristic (110), (200), (310) and (211) peaks (blue pattern in Figure 4a).[67] Lattice constants were calculated to be a = 9.78 Å and c = 2.85 Å, also in good agreement with those reported for α-MnO_2 (a = 9.78 Å and c = 2.86 Å).[68] The α-MnO_2 found in experiments is different than the more thermodynamically stable β-MnO_2(110) used in our DFT work. Because PXRD informs on bulk but not surface structure, we studied here the most thermodynamically stable surface structure with DFT, β-MnO_2(110). Additional details are given in ESI for $Co(ClO_4)_2$ and $Ni(ClO_4)_2$. Overall, PXRD supports our conclusion that the origin of the humid O_3-triggered change in orientation of 5CB on the three metal salts is oxidation of metal cations to their oxides or oxyhydroxides (indicated by the green bars in Figure 2).

3.3 Selectivity

The computational and experimental results presented above support our conclusion that humid O_3 can trigger LCs to undergo orientational transitions on perchlorate surfaces of Mn^{2+}, Co^{2+}, and Ni^{2+} due to the strongly exergonic reaction free energies (ΔG < -0.67 eV in Table S3) and associated change in LC binding free energies (Tables 1 and 2). In addition, our conclusions are supported by the observation that there is no response to humid O_3 on Al^{3+} because Al is already in its highest oxidation state.

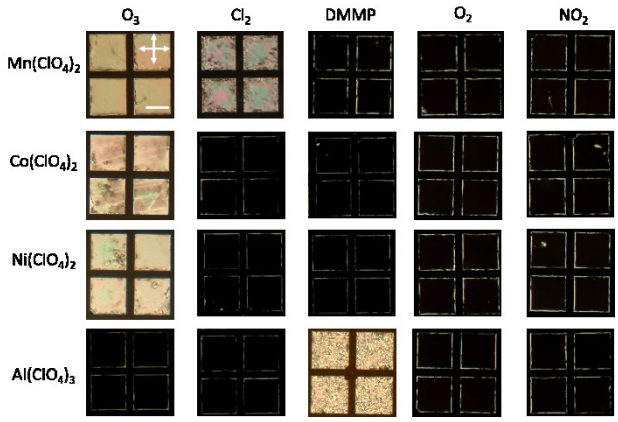

Figure 5. Optical images (crossed polarizers) of 5CB hosted in copper grids on surfaces decorated with ~15 pmol/mm^2 $Mn(ClO_4)_2$, $Co(ClO_4)_2$, $Ni(ClO_4)_2$, or $Al(ClO_4)_3$ after exposure to humid 4±1 ppm O_3, 5±0.2 ppm Cl_2, 5 ppm DMMP, 20 vol% O_2, or 5 ppm NO_2 for 1 hour; humidity is 20% RH. The scale bar is 200 µm.

Here we discuss a strategy that permits selective responses to O_3 and Cl_2. The strategy for selective LC response is based on surfaces that display multiple types of metal cations, each patterned at distinct spatial locations. Specifically, previously we reported that 5CB supported on $Mn(ClO_4)_2$ responded to Cl_2 but that no response was recorded when the LC was supported on $Al(ClO_4)_3$ or $Ni(ClO_4)_2$.[27] Additionally, as shown in Figure 5, LCs supported on Co^{2+} do not respond to Cl_2. Because it is possible to trigger a LC anchoring transition with O_3 on Ni^{2+} and Co^{2+}, these observations suggest that Cl_2 is not sufficiently strong to oxidize Ni^{2+} or Co^{2+}. This interpretation was confirmed by PXRD measurements (Figure S7), which revealed that there is no significant change in the crystal structure of bulk $Ni(ClO_4)_2$ or $Co(ClO_4)_2$ salt upon exposure to Cl_2. In contrast, for Cl_2-exposed to $Mn(ClO_4)_2$, the PXRD pattern is similar to that of O_3-exposed $Mn(ClO_4)_2$ indicating the formation of MnO_2 (Figure S7).

Inspection of Figure 5 reveals that the above considerations enable the design of a chemoresponsive LC system that can selectively detect O_3 or Cl_2 in the presence of O_2 and NO_2. Specifically, the LC supported on Mn^{2+} responds to both O_3 and Cl_2, but the LC supported on Co^{2+} or Ni^{2+} will indicate if this gas is O_3 (response) or Cl_2 (no response). We note here that the optical responses of the LCs to O_3 and Cl_2 are not reversed by subsequent exposure to dry N_2 or reducing gases (e.g., dry 2% H_2 or 2% CO in N_2) for 1 hr. Our conclusion is that the metal oxide or oxyhydroxides formed during the LC response are not reduced at room temperature. Prior examples of reduction of MnO_2 by using CH_4-H_2 required use of temperatures of over 1000°C.[69] The irreversible optical response makes these designs of chemoresponsive LCs potentially suitable for use in sensors that (1) alarm upon exposure to a threshold concentration of gas, or (2) measure cumulative exposure to a gas (e.g., dosimeters). Additionally, we characterized the response of LC supported on these three metal salts to common potentially interfering oxidizing agents such as oxygen gas (20 v%) in air and NO_2 (8 ppm) at 20% RH. These measurements revealed no measurable response of the metal salt-supported LC to these gases. The experimental results obtained with oxygen and NO_2 are consistent with reaction free energies shown Figure 2 and Table S3, which reveal that oxidation of the three metal salts by O_2 and NO_2 is not thermodynamically favored based on reaction free energies (the agreement between calculated reaction free energy and experimental observation is denoted by the green bars in Figure 2).

We make two additional comments regarding our design of a chemoresponsive LC system for selective detection of Cl_2 and O_3. First, a comparison of the Cl_2 experiments to the reaction free energies in Figure 2 suggests that the DFT calculations do not, at first inspection, predict the experimental observations. For example, all reaction free energies in Figure 2 for Cl_2 gas on Co^{2+}, Mn^{2+}, and Ni^{2+} are negative, which indicates that thermodynamics allows the oxidation of all these cations by Cl_2. In contrast, we observe LC responses in experiments when using Mn^{2+} but not Co^{2+} or Ni^{2+} (Figure 5). As noted above, however, these predicted reaction free energies are within 0.15 eV of zero, which suggests that this disagreement could be due to DFT error (mean absolute error for DFT adsorption on transition metal surface tends to be ~0.2 eV but greater for some cases[70]).

While the absolute error is 0.15 eV, the relative error is smaller. For example, we calculate that the reaction free energy to form MnO_2 is only 0.04 eV less favored than the formation of NiOOH with Cl_2. In addition, this analysis neglects kinetics, which can also play a role in the experimental results. However, we are not aware of experimental evidence in literature describing a reaction of Cl_2 with Co^{2+} or Ni^{2+} at room temperature. We obtain the best agreement between experiment and calculated reaction free energies if the threshold reaction free energy is set at -0.15 eV in Figure 2.

Second, as shown in Figure 5, it is possible to extend the scope of targeted chemical compound detected by chemoresponsive LCs supported on an array of metal salts by including additional metal cations[26]. Specifically, the inclusion of a surface region decorated with Al^{3+} will enable selective detection of DMMP only. The design builds from prior reports in which we have studied Mn^{2+}, Co^{2+}, Ni^{2+}, and Al^{3+} perchlorate systems with 5CB for DMMP detection using the displacement mechanism.[5,20–22] For these systems, DMMP triggers an anchoring transition in 5CB on $Al(ClO_4)_3$ but not Co^{2+}, Ni^{2+}, or Mn^{2+}. As noted above, $Al(ClO_4)_3$ is not oxidized by Cl_2 or O_3, which means that selectivity between oxidizing agents and DMMP is easily achieved (Table 2) by using $Al(ClO_4)_3$. Overall, this last observation illustrates the point that patterning of judiciously selected metal cations on surfaces is a strategy that can enable the design of chemoresponsive LCs capable of selectively reporting the presence of multiple targeted chemical species.

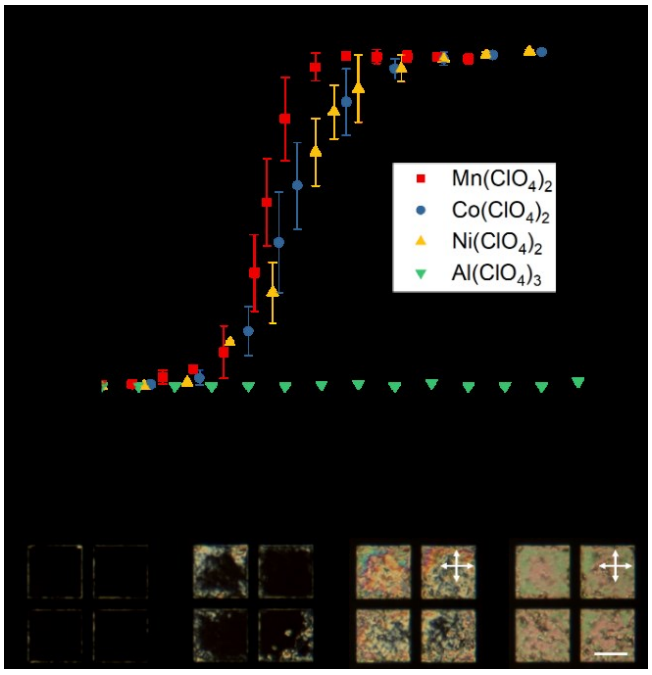

Figure 6. (a) Normalized intensity of polarized light transmitted through 5CB supported on surfaces decorated with 15±3 pmol/mm^2 $Mn(ClO_4)_2$, 15±2 pmol/mm^2 $Ni(ClO_4)_2$, 16±3 pmol/mm^2 $Co(ClO_4)_2$, and 16±3 pmol/mm^2 $Al(ClO_4)_3$ exposed to 1290±40 ppm O_3 gas at 20% RH. (b) Optical images of 5CB (crossed polarizers) on 15±3 pmol/mm^2 $Mn(ClO_4)_2$ recorded 0, 20, 30 and 50 seconds after initial exposure to 1290±40 ppm O_3 gas at 20% RH. The scale bar is 200 µm.

3.4 Response dynamics of LC to O_3 gas

Next, we characterized the dynamics of the optical responses of nematic 5CB films supported on $Mn(ClO_4)_2$-, $Co(ClO_4)_2$- and

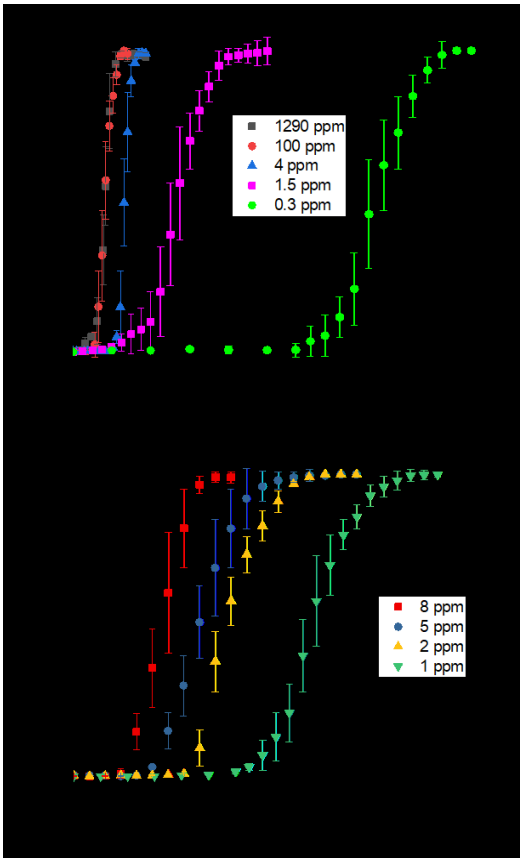

Figure 7. Normalized intensity of polarized light transmitted through 5CB supported on surface decorated with 15±3 pmol/mm^2 $Mn(ClO_4)_2$ exposed to (a) O_3 at 1290±40, 100±10, 4±1, 1.5±0.2, and 0.3±0.1 ppm and (b) Cl_2 at 8±0.3, 5±0.2, 2±0.1, and 1±0.1 ppm with 20% RH.

$Ni(ClO_4)_2$-decorated surfaces to humid O_3 gas. Initially, the 5CB adopted a homeotropic orientation, leading to a dark appearance through crossed polarizers (defined as a normalized light intensity of zero in Figure 6a). After flowing 1290±40 ppm O_3 gas with 20% RH over the LC samples, as shown in Figure 6b, we observed a dynamic orientational transition starting ~20 seconds after the onset of exposure. With increasing duration of exposure to O_3 gas, we observed an increase in the brightness of the LC, eventually leading to a uniformly bright LC film (defined as a normalized light intensity of one in Figure 6a). The continuous change in interference colors during O_3 exposure indicates a continuous LC anchoring transition (LC molecules are tilting). In contrast, $Al(ClO_4)_3$-decorated surfaces, which are not oxidized by humid O_3 gas, show no measurable orientational response (Figure 6a, green triangles).

To examine the dependence of the LC dynamic response to O_3 gas concentration, we exposed 5CB on 15±3 pmol/mm^2 $Mn(ClO_4)_2$-decorated glass surfaces to humid (20% RH) O_3 concentrations (Figure 7a) of 100±10, 4±1, 1.5±0.2, and 0.3±0.1 ppm (obtained by changing the O_2-to-N_2 ratio in the gas source fed to the ozone generator). As shown in Figure 7a, we observed similar dynamic responses of the LC upon exposure to 1290±40 ppm and 100±10 ppm O_3 with 20% RH but slower LC response

for the lower O_3 concentrations (4±1, 1.5±0.2, and 0.3±0.1 ppm). In addition to use of 20% RH, we also tested the response of 5CB on $Mn(ClO_4)_2$ to 4±1 ppm O_3 with 10% or 60% RH. There was no measurable influence of humidity on the response time to O_3 (Table S5). For comparison, we also measured the concentration-dependent response of the same LC system to Cl_2 at 8±0.3, 5±0.2, 2±0.1, and 1±0.1 ppm with 20% RH (Figure 7b).

To provide insight into the dynamic response of the LC shown in Figure 7, we developed a simple transport-reaction model.[50] The model assumes that any analyte molecule that diffuses to the metal cation-decorated surface immediately reacts, making the process diffusion-limited and independent of the reaction kinetics and thermodynamics (Figure 8a). Inspection of Figure 8a shows that the analyte diffuses through both a vapor phase concentration boundary layer and a LC layer with thickness δ_{Air} and δ_{LC}, respectively. As detailed in ESI, we fit our transport-reaction model to experimental measurements of the dynamic LC response to Cl_2 and O_3 (Figure 8b,c). The comparison of the model and experimental measurements revealed that the dynamic response of the LC to both O_3 and Cl_2 is rate-limited by diffusion across the LC film. To test these conclusions, we changed the LC thickness from 18 µm to 30 µm. When using 100 ppm O_3, consistent with our conclusions, we observed the LC response time to increase from 17 s to 26 s (for a response corresponding to 10% of the normalized light intensity). Overall, these results suggest that the process controlling the dynamic LC response to these analytes differs from the previously studied case of DMMP detection on $Al(ClO_4)_3$, where it was found that diffusion was limited on the air side. As detailed in the ESI, this difference arises from the analyte-specific partition coefficients between air and the LC.

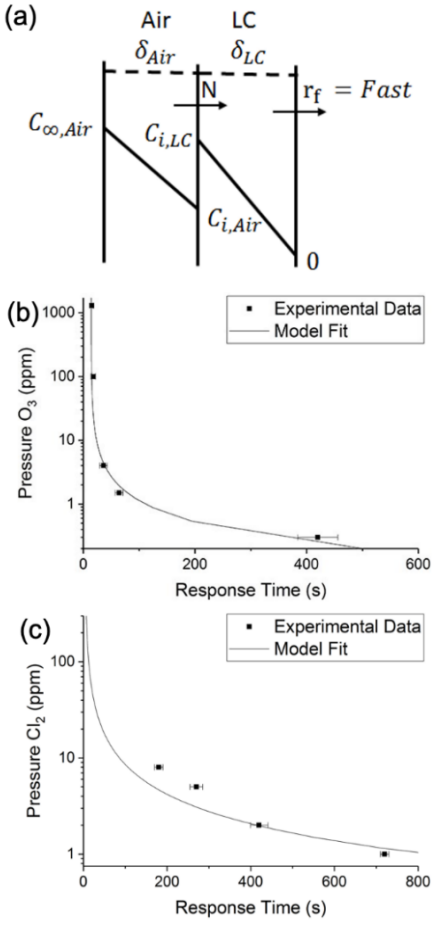

Figure 8. (a) Schematic illustration of the concentration profile of an oxidant with flux N as it diffuses from air ($C_{\infty,Air}$) across a film of LC to a reactive surface. The concentration on the air side of the air-LC interface is defined as $C_{i\,Air}$ and the concentration on the LC side is defined as $C_{i\,5CB}$. The experimental data and the fittings using the above described model for the response times of 5CB on 15±3 pmol/mm^2 $Mn(ClO_4)_2$ decorated surface to (b) 1290±40, 100±10, 4±1, 1.5±0.2, and 0.3±0.1 ppm O_3 with 20% RH and (c) 8±0.3, 5±0.2, 2±0.1, and 1±0.1 ppm Cl_2 with 20% RH. The response time was defined as the time required to reach 10% normalized light intensity in Figure

4. Conclusions

This paper reports validation of a design methodology that leads to chemically selective LC materials that can distinguish O_3 and Cl_2 at ppb concentrations. We combined electronic structure calculations and experiments to show that Mn^{2+}, Co^{2+}, and Ni^{2+} cations can serve as surface binding sites that undergo redox-triggered changes in strength of binding to nitrile-containing LC materials upon exposure to humid O_3. Specifically, by selecting the metal cation species on the basis of calculations of reaction free energies from first-principles computations, we were able to demonstrate a strategy for selective responses to humid O_3 and Cl_2 based on patterning of the metal cations on surfaces. We also developed a kinetic model to describe the dynamics of the LC orientational transitions on $Mn(ClO_4)_2$ following exposure to humid O_3 and Cl_2, and found that the rate-limiting process governing the response of the LC is mass transfer of these species across the LC. These results are conceptually important because they demonstrate it is possible to leverage first-principles insights regarding chemical reactions at interfaces to design both equilibrium and dynamic properties of stimuli-responsive materials.

Our results also generate a range of questions: (i) Are the metal salt layers fully oxidized to their oxides/oxyhydroxides or just the outer layers?; (ii) How does humidity or O_3 concentration in the gas stream change spatial patterns and time-dependent interference colors exhibited by the LC; (iii) How does the LC respond if O_3 and Cl_2 are mixed in a gas stream? We envisage a range of future directions of investigation to address these and other questions. For example, machine learning (ML) frameworks have been used to analyze and uncover valuable feature information in LC responses,[71,72] and they could be used to identify informative features that provide insight into the underlying phenomena that governs and distinguishes LC responses to humid O_3 and Cl_2. We also envision that the principles outlined in this work can be extended to the detection of reducing agents[73–75], such as H_2, CO, NH_3 and NO.

Conflicts of interest

N.L.A. declares a financial interest in Platypus Technologies LLC, a for-profit company that has developed LC-based analytic technologies.

Acknowledgements

This work was supported by the National Science Foundation (DMREF grant: DMR-1921696, DMR-1921722, and DMR-1921668) and the Army Research Office (W911NF-14-1-0140). Part of the computational work conducted by J.G. and M.M. in this study was carried out through external computational facilities at: the DoD High Performance Computing Modernization Program (US Air Force Research Laboratory DoD Supercomputing Resource Center (AFRL DSRC), the US Army Engineer Research and Development Center (ERDC), and the Navy DoD Supercomputing Resource Center (Navy DSRC), ARONC43623362), supported by the Department of Defense; and the National Energy Research Scientific Computing Center (NERSC) through the U.S. DOE, Office of Science under Contract No. DE-AC02-05CH11231; X-ray powder diffraction (XRPD) measurements were performed in Cornell Center for Materials Research (CCMR), supported by the NSF Grant DMR-1719875, part of the NSF MRSEC Program.

References

1 F. Reinitzer, *Monatshefte für Chemie*, 1888, **9**, 421–441.
2 V. Fréedericksz and V. Zolina, *Trans. Faraday Soc.*, 1933, **29**, 919–930.
3 H. Kawamoto, *Proc. IEEE*, 2002, **90**, 460–500.
4 J. M. Brake, M. K. Daschner, Y. Y. Luk and N. L. Abbott, *Science*, 2003, **302**, 2094–2097.
5 R. R. Shah and N. L. Abbott, *Science*, 2001, **293**, 1296–1299.
6 R. J. Carlton, J. T. Hunter, D. S. Miller, R. Abbasi, P. C. Mushenheim, L. N. Tan and N. L. Abbott, *Liq. Cryst. Rev.*, 2013, **1**, 29–51.
7 S. J. Woltman, G. D. Jay and G. P. Crawford, *Nat. Mater.*, 2007, **6**, 929–938.
8 F. L. Dickert, U. P. A. Bäumler and G. K. Zwissler, *Synth. Met.*, 1993, **61**, 47–52.
9 H. Yokoyama, *Mol. Cryst. Liq. Cryst. Inc. Nonlinear Opt.*, 1988, **165**, 265–361.
10 B. Jerome, *Reports Prog. Phys.*, 1991, **54**, 391–451.
11 R. R. Shah and N. L. Abbott, *Langmuir*, 2003, **19**, 275–284.
12 S. K. Pal, C. Acevedo-Vélez, J. T. Hunter and N. L. Abbott, *Chem. Mater.*, 2010, **22**, 5474–5482.
13 P. Cachelin, J. P. Green, T. Peijs, M. Heeney and C. W. M. Bastiaansen, *Adv. Opt. Mater.*, 2016, **4**, 592–596.
14 M. A. Bedolla Pantoja and N. L. Abbott, *ACS Appl. Mater. Interfaces*, 2016, **8**, 13114–13122.
15 V. J. Aliño, P. H. Sim, W. T. Choy, A. Fraser and K. L. Yang, *Langmuir*, 2012, **28**, 17571–17577.
16 T. Govindaraju, P. J. Bertics, R. T. Raines and N. L. Abbott, *J. Am. Chem. Soc.*, 2007, **129**, 11223–11231.
17 V. K. Gupta, J. J. Skaife, T. B. Dubrovsky and N. L. Abbott, *Science*, 1998, **279**, 2077–2080.
18 S. M. Malone and D. K. Schwartz, *Langmuir*, 2011, **27**, 11767–11772.
19 C. H. Jang, M. L. Tingey, N. L. Korpi, G. J. Wiepz, J. H. Schiller, P. J. Bertics and N. L. Abbott, *J. Am. Chem. Soc.*, 2005, **127**, 8912–8913.
20 K. Yang, K. Cadwell and N. L. Abbott, *J. Phys. Chem. B*, 2004, **108**, 20180–20186.
21 J. T. Hunter, S. K. Pal and N. L. Abbott, *ACS Appl. Mater. Interfaces*, 2010, **2**, 1857–1865.
22 T. Szilvási, N. Bao, H. Yu, R. J. Twieg, M. Mavrikakis and N. L. Abbott, *Soft Matter*, 2018, **14**, 797–805.
23 K. Nayani, P. Rai, N. Bao, H. Yu, M. Mavrikakis, R. J. Twieg and N. L. Abbott, *Adv. Mater.*, 2018, **30**, 1–7.
24 H. Yu, T. Szilvási, P. Rai, R. J. Twieg, M. Mavrikakis and N. L. Abbott, *Adv. Funct. Mater.*, 2018, **28**, 1703581.
25 T. Szilvási, L. T. Roling, H. Yu, P. Rai, S. Choi, R. J. Twieg, M. Mavrikakis and N. L. Abbott, *Chem. Mater.*, 2017, **29**, 3563–3571.
26 J. I. Gold, T. Szilvási, N. L. Abbott and M. Mavrikakis, *ACS Appl. Mater. Interfaces*, 2020, **12**, 30941-30953.
27 T. Szilvási, N. Bao, K. Nayani, H. Yu, P. Rai, R. J. Twieg, M. Mavrikakis and N. L. Abbott, *Angew. Chemie Int. Ed.*, 2018, **57**, 9665–9669.
28 M. C. Collivignarelli, A. Abbà, I. Benigna, S. Sorlini and V. Torretta, *Sustain.*, 2016, **69**, 157-168.
29 L. Varga and J. Szigeti, *Int. J. Dairy Technol.*, 2016, 157–168.
30 Z. B. Guzel-Seydim, A. K. Greene and A. C. Seydim, *LWT - Food Sci. Technol.*, 2004, **37**, 453–460.
31 W. Bruening and F. J. M. Concha, *J. Chromatogr. A*, 1975, **112**, 253–265.
32 T. Doll, J. Lechner, I. Eisele, K. D. Schierbaum and W. Göpel, *Sensors Actuators, B Chem.*, 1996, **34**, 506–510.
33 X. Pang, M. D. Shaw, A. C. Lewis, L. J. Carpenter and T. Batchellier, *Sensors Actuators, B Chem.*, 2017, **240**, 829–837.
34 M. C. Carotta, A. Cervi, A. Fioravanti, S. Gherardi, A. Giberti, B. Vendemiati, D. Vincenzi and M. Sacerdoti, *Thin Solid Films*, 2011, **520**, 939–946.
35 M. Belaqziz, M. Amjoud, A. Gaddari, B. Rhouta and D. Mezzane, *Superlattices Microstruct.*, 2014, **71**, 185–189.
36 A. Bejaoui, J. Guerin, J. A. Zapien and K. Aguir, *Sensors Actuators, B Chem.*, 2014, **190**, 8–15.
37 J. Ollitrault, N. Martin, J. Y. Rauch, J. B. Sanchez and F. Berger, *Mater. Lett.*, 2015, **155**, 1–3.
38 C. Esteves, E. Ramou, A. R. P. Porteira, A. J. Moura Barbosa and A. C. A. Roque, *Adv. Opt. Mater.*, 2020, **8**, 1902117.
39 V. V. Klemas, *J. Coast. Res.*, 2015, **31**, 1260–1267.
40 M. S. Hussain and S. Farooq, *J. Environ. Sci. Heal. Part A Environ. Sci. Eng.*, 1989, **24**, 389–407.
41 R. Andreozzi, A. Insola, V. Caprio and M. G. D'Amore, *Water Res.*, 1992, **26**, 917–921.
42 F. Jacobsen, J. Holcman and K. Sehested, *Int. J. Chem. Kinet.*, 1998, **30**, 207–214.
43 N. Kijima, H. Yasuda, T. Sato and Y. Yoshimura, *J. Solid State Chem.*, 2001, **159**, 94–102.
44 G. R. Hill, *J. Am. Chem. Soc.*, 1949, **71**, 2434–2435.
45 T. Nishimura and Y. Umetsu, *Hydrometallurgy*, 1992, **30**, 483–497.
46 Q. H. Tian, X. Y. Guo, Y. Yi and Z. H. Li, *Trans. Nonferrous Met. Soc. China (English Ed.)*, 2010, **20**, s42–s45.
47 A. V. Levanov, O. Y. Isaikina and V. V. Lunin, *Russ. J. Phys. Chem. A*, 2016, **90**, 2358–2363.

48 F. Bardé, M. R. Palacin, B. Beaudoin, A. Delahaye-Vidal and J. M. Tarascon, *Chem. Mater.*, 2004, **16**, 299–306.

49 F. Bardé, M. R. Palacín, B. Beaudoin and J. M. Tarascon, *Chem. Mater.*, 2005, **17**, 470–476.

50 J. T. Hunter and N. L. Abbott, *Sensors Actuators, B Chem.*, 2013, **183**, 71–80.

51 G. Kresse and J. Furthmüller, *Comput. Mater. Sci.*, 1996, **6**, 15–50.

52 G. Kresse and J. Furthmüller, *Phys. Rev. B - Condens. Matter Mater. Phys.*, 1996, **54**, 11169–11186.

53 P. E. Blöchl, *Phys. Rev. B*, 1994, **50**, 17953–17979.

54 D. Joubert, *Phys. Rev. B - Condens. Matter Mater. Phys.*, 1999, **59**, 1758–1775.

55 J. P. Perdew, K. Burke and M. Ernzerhof, *Phys. Rev. Lett.*, 1996, **77**, 3865–3868.

56 S. Grimme, J. Antony, S. Ehrlich and H. Krieg, *J. Chem. Phys.*, 2010, **132**, 154104.

57 a. I. Lichtenstein, V. I. Anisimov and J. Zaanen, *Phys. Rev. B*, 1995, **52**, 5467–5471.

58 V. I. Anisimov, J. Zaanen and O. K. Andersen, *Phys. Rev. B*, 1991, **44**, 943–954.

59 Y. F. Li and A. Selloni, *ACS Catal.*, 2014, **4**, 1148–1153.

60 C. Sun, Y. Wang, J. Zou and S. C. Smith, *Phys. Chem. Chem. Phys.*, 2011, **13**, 11325–11328.

61 S. Selcuk and A. Selloni, *J. Phys. Chem. C*, 2015, **119**, 9973–9976.

62 J. D. Pack and H. J. Monkhorst, *Phys. Rev. B*, 1977, **16**, 1748–1749.

63 L. T. Roling, J. Scaranto, J. A. Herron, H. Yu, S. Choi, N. L. Abbott and M. Mavrikakis, *Nat. Commun.*, 2016, **7**, 13338.

64 D. R. Lide, *CRC Handbook of Chemistry and Physics*, Boca Raton, 84th edn., 2004.

65 O. J. Hao, A. P. Davis and P. H. Chang, *J. Environ. Eng. (United States)*, 1991, **117**, 359–374.

66 M. Deborde and U. von Gunten, *Water Res.*, 2008, **42**, 13–51.

67 L. Feng, Z. Xuan, H. Zhao, Y. Bai, J. Guo, C. wei Su and X. Chen, *Nanoscale Res. Lett.*, 2014, **9**, 1–8.

68 C. Masquelier, M. Tabuchi, K. Ado, R. Kanno, Y. Kobayashi, Y. Maki, Ţ Osamu Nakamura, J. B. Goodenough, L. ƨ LiMn and Ä Li, *J. Solid State Chem.*, 1996, **123**, 255–266.

69 B. Liu, Y. Zhang, Z. Su, Z. Peng, G. Li and T. Jiang, *Jom*, 2017, **69**, 1669–1675.

70 J. Wellendorff, T. L. Silbaugh, D. Garcia-Pintos, J. K. Nørskov, T. Bligaard, F. Studt and C. T. Campbell, *Surf. Sci.*, 2015, **640**, 36–44.

71 Y. Cao, H. Yu, N. L. Abbott and V. M. Zavala, *ACS Sensors*, 2018, **3**, 2237–2245.

72 A. Smith, N. Abbott and V. M. Zavala, *ChemRxiv*.

73 G. B. Taylor and H. W. Starkweather, *J. Am. Chem. Soc.*, 1930, **52**, 2314–2325.

74 N. Yamamoto, S. Tonomura, T. Matsuoka and H. Tsubomura, *Jpn. J. Appl. Phys.*, 1981, **20**, 721–726.

75 J. Li, H. Chang, L. Ma, J. Hao and R. T. Yang, *Catal. Today*, 2011, **175**, 147–156.